Journal of
Biomedical Optics

BiomedicalOptics.SPIEDigitalLibrary.org

Determination of optical properties of human tissues obtained from parotidectomy in the spectral range of 250 to 800 nm

Eric L. Wisotzky
Florian C. Uecker
Steffen Dommerich
Anna Hilsmann
Peter Eisert
Philipp Arens

Eric L. Wisotzky, Florian C. Uecker, Steffen Dommerich, Anna Hilsmann, Peter Eisert, Philipp Arens, "Determination of optical properties of human tissues obtained from parotidectomy in the spectral range of 250 to 800 nm," *J. Biomed. Opt.* **24**(12), 125001 (2019), doi: 10.1117/1.JBO.24.12.125001.

Journal of Biomedical Optics 24(12), 125001 (December 2019)

Determination of optical properties of human tissues obtained from parotidectomy in the spectral range of 250 to 800 nm

Eric L. Wisotzky,[a,b,*,†] **Florian C. Uecker,**[c,†] **Steffen Dommerich,**[c] **Anna Hilsmann,**[a] **Peter Eisert,**[a,b] **and Philipp Arens**[c,*]
[a]Fraunhofer Heinrich-Hertz-Institute, Computer Vision and Graphics, Berlin, Germany
[b]Humboldt-Universität zu Berlin, Visual Computing, Berlin, Germany
[c]Charité—Universitätsmedizin Berlin, Department of Otorhinolaryngology, Berlin, Germany

Abstract. The optical properties of human tissues are an important parameter in medical diagnostics and therapy. The knowledge of these parameters can encourage the development of automated, computer-driven optical tissue analysis methods. We determine the absorption coefficient μ_a and scattering coefficient μ_s' of different tissue types obtained during parotidectomy in the wavelength range of 250 to 800 nm. These values are determined by high precision integrating sphere measurements in combination with an optimized inverse Monte Carlo simulation. To conserve the optical behavior of living tissues, the optical spectroscopy measurements are performed immediately after tissue removal. Our study includes fresh samples of the ear, nose, and throat (ENT) region, as muscle tissue, nervous tissue, white adipose tissue, stromal tissue, parotid gland, and tumorous tissue of five patients. The measured behavior of adipose corresponds well with the literature, which sustains the applied method. It is shown that muscle is well supplied with blood as it features the same characteristic peaks at 430 and 555 nm in the absorption curve. The parameter μ_s' decreases for all tissue types above 570 nm. The accuracy is adequate for the purposes of providing μ_a and μ_s' of different human tissue types as muscle, fat, nerve, or gland tissue, which are embedded in large complex structures such as in the ENT area. It becomes possible for the first time to present reasonable results for the optical behavior of human soft tissue located in the ENT area and in the near-UV, visual, and near-infrared areas. [DOI: 10.1117/1.JBO.24.12.125001]

Keywords: optical properties; absorption coefficient; scattering coefficient; Monte Carlo simulation; parotidectomy.

Paper 190212R received Jun. 25, 2019; accepted for publication Nov. 7, 2019; published online Dec. 3, 2019.

1 Introduction

The optical properties of human tissues have an effect on many diagnostic and therapeutic applications in laser medicine, but they are also important for routine medical diagnostics. Light can penetrate and then escape tissue, which increases the interest in understanding the scattering and absorption properties of human tissues, as it is the basis for medical diagnostics and therapy.[1] Specifying the optical properties of human tissue is the initial step in interpreting measurements correctly. These properties can then be used to predict the light distribution and deposition in tissue for many applications, e.g., intraoperative tissue analysis.

Knowledge of *in-vivo* optical tissue properties can encourage the development of automatic optical tissue analysis methods. For example, computer-driven optical tissue analysis has a huge potential in diagnostic medicine and surgery. Surgeons use microscopes, endoscopes, high-definition cameras, and other devices for a better differentiation between different tissues during surgery. Computer-aided detection and augmentation of sensible structures and tissues could lead to better results and more reliability in surgical procedures, especially in the head and neck region, with many sensible structures present.[2,3]

For endoscopy-driven surgeries, the narrowband imaging technique of blood vessels in mucosal structures has proven the potential of using wavelength-filtered light to enhance the diagnostic outcome of visual patient data.[4] This technique uses light in the visual range. Broader knowledge of optical tissue properties could lead to new tools for other surgically relevant structures such as, for instance, nerves or tumor tissue.

Various authors have analyzed optical properties of several different human tissue types, such as different skin types and layers, blood, brain, breast, bone, liver, kidney, lung, muscle, and fatty tissues.[1,5] These tissue types, except for muscle, have in common that they are easily distinguishable from surrounding tissues and thus are relatively easy to extract. Except for blood and skin, where extensive data are available, most studies mainly analyze a few data points in a relatively narrow wavelength range, mainly in the infrared (IR). These results, however, are usually not applicable to intraoperative usage, as tissue there is illuminated in the visual range from 400 to 700 nm.

Furthermore, most of these measurements have been performed *ex vivo*. The *in-vivo* optical properties of tissues, however, are substantially different, as living tissue is subject to influences of blood, water, and collagen content as well as fiber development.[6] These influences, e.g., the amount of blood that infiltrates the specific tissue types or the tissue-specific water content, differ from tissue type to tissue type as well as from patient to patient.

---

*Address all correspondence to Eric L. Wisotzky, E-mail: eric.wisotzky@hhi.fraunhofer.de; Philipp Arens, E-mail: philipp.arens@charite.de

†Eric L. Wisotzky and Florian C. Uecker contributed as joint first authors.

The most common method of quantifying optical properties in the ultraviolet (UV), visual, and IR spectral range of biochemical systems is optical absorption spectroscopy.[7] The optical properties of a tissue sample are described by the intrinsic optical parameters absorption coefficient μ_a (mm^{-1}), scattering coefficient μ_s (mm^{-1}), and the scattering phase function represented by the anisotropy factor g.[8] These parameters characterize tissue scattering in terms of the relative forward versus backward direction of scatter for thicker tissue samples (with multiple scattering events). An introduction to the optical properties is presented in Ref. 9.

The aim of this study is to derive a set of empirical formulations to predict the optical properties of different types of human soft tissue in the anatomical region of ear, nose, and throat (ENT). Different kinds of fatty and muscle tissue have been already examined.[10–14] But to the best of our knowledge, the optical parameters μ_a, μ_s, g, and μ_s' of other human ENT soft tissues, such as nerve and gland tissues, are currently not available.[1,5] This work determines muscle, nervous, white adipose, and stromal tissues as well as parotid gland and tumorous tissues, extracted during parotidectomy. An improved integrating sphere technique combined with inverse Monte Carlo simulations (iMCS)[15–17] is used to determine the optical parameter μ_a, μ_s, and g of the tissue samples. An experimental setup is used that provides transmittance and reflectance measurements in the wavelength range from 250 to 800 nm under defined conditions.

2 Material and Methods

2.1 *Patients*

This study has been conducted with five patients, aged between 57 and 86 years. The patients had a parotid gland tumor and needed a conventional parotidectomy. The parotid gland is located anterior inferior to the ear (see Fig. 1) and is the largest of the three groups of paired large salivary glands. It is surrounded by fat, muscle, and stromal tissues. The gland itself is composed of a superficial lobe and a deep lobe divided by the posterior facial vein and facial nerve. During surgery of parotid gland tumors, the greatest difficulty is the extirpation of the entire tumor with safety margins while protecting the facial nerve. Patients' written informed consent for extracting healthy samples of muscle tissue, nervous tissue (N. auricularis magnus, which is located next to the gland), white adipose tissue, stromal tissue, and parotid gland as well as tumorous tissue during the standard procedure have been provided. The tissues are extracted individually, selected during the surgery by the clinician. As local anatomy (cf. Fig. 1) and specific area of intervention differ from patient to patient, not all tissue types could be extracted from all patients. Table 1 shows the different extracted tissue types for each patient. In our study, we took a sample from a cystadenolymphoma. This benign tumor was located in the superficial lobe of the parotid gland and is the second most common salivary gland tumor. Generally, 64% to 80% of all salivary gland tumors occur in the parotid gland. Most of them are located in the superficial lobe in the parotid gland.[18] Due to the individual anatomy of each patient, the amount of extracted tissue differed as well, leading to different sample thicknesses d. After spectroscopy, all taken samples are additionally analyzed using normal histological examination to confirm the specific tissue type. The whole study is in agreement with the ethical approval obtained from the ethics committee of the Charité–Universitätsmedizin Berlin.

Table 1 The extracted tissue types for each patient. The tissue type is confirmed by a histological examination after spectral analysis.

	Tissue type					
	Fat	Muscle	Parotid gland	Nerve	Stromal	Tumor
Patient 1	X	X	X	X	—	—
Patient 2	X	X	X	X	—	—
Patient 3	—	X	X	X	—	X
Patient 4	—	—	X	—	X	—
Patient 5	X	—	X	—	—	—

2.2 *Spectroscopic Measurements*

The tissue probes are prepared directly after being removed from the patient to fit on the cuvette, with a measured thickness

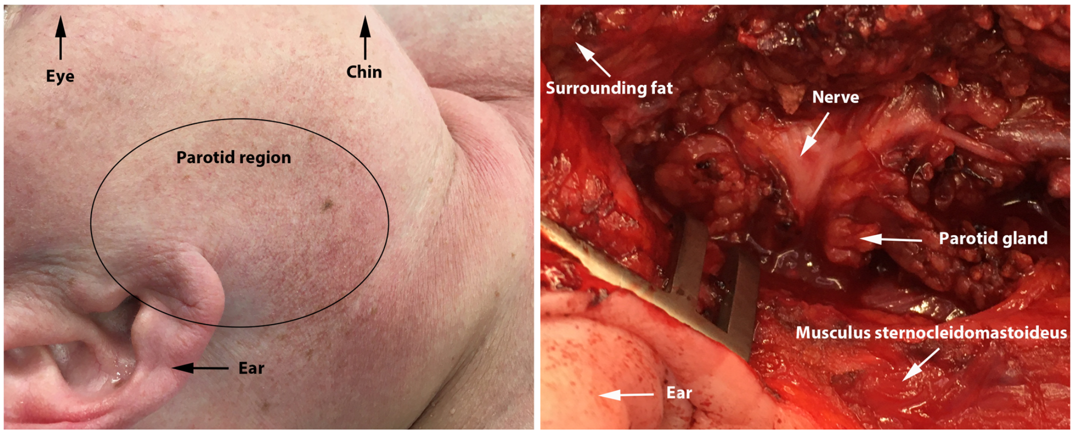

(a) (b)

Fig. 1 (a) Location and (b) anatomy of the interventions. An open situs, where all relevant tissue structures are visible, is shown in (a). The position of this situs is shown in (b) marked with parotid region.

between 103 and 551 μm, depending on the sample quantity. The diameter of the prepared probes is between 6.0 and 15.0 mm. Most measurements were taken in the first two hours after removal to obtain the optical properties of living tissue. To show the effect of degeneration and its influence on the optical behavior, four probes are additionally analyzed at different time instants t. The macroscopic optical parameters, diffuse reflectance R_d, and the total transmission T_t are measured every 5 nm in the spectral range from 250 to 800 nm, with an integrating sphere UV/visible spectrophotometer (Lambda 650, PerkinElmer, Germany), which is a two-beam spectrometer with double monochromator system. This leads to 111 datasets per measurement. The diameter of the incident light beam on the tissue sample is 4.5 mm and the scan rate is 5 nm/s. A schematic representation of the sphere setup used in this study can be found in the work by Friebel et al.[15] in Fig. 1.

The light source consists of a deuterium lamp for the UV range and a wolfram halogen lamp for the visible/near-infrared (VIS/NIR) range. The cuvette can be fixed in a defined position at a constant distance to the sphere aperture in front of or behind the integrating sphere to measure the transmittance spectra T_t or the reflectance spectra R_d, respectively. For the measurement of T_t, the reflectance port is closed with a diffuse reflecting Spectralon® standard with a known reflectance spectrum. Here R_d is measured relative to the reflectance standard by replacing the special Spectralon® by the sample. The Fresnel reflectance of the cuvette glass leaves the sphere through the open Fresnel port to avoid interference with the diffuse reflectance. This spectrophotometric setup allows the measurement of macroscopic radiation distribution with an extremely reduced error potential.[15]

2.3 *Inverse Monte Carlo Simulation*

The optical parameters μ_a and $\mu_s' = \mu_s(1-g)$ are obtained from the iMCS. The iMCS method, first presented by Roggan,[19] is adapted to the geometry of the measurement system[15] and uses iteratively forward Monte Carlo simulation to calculate μ_a, μ_s, and g from the measured reflection R_d and transmission T_t using a phase function.[8] For initialization, the iMCS uses estimated μ_a, μ_s, and g from the Kubelka–Munk theory.[15] The forward simulation uses the Newton–Raphson method[20] to find an approximation of $R_d(\mu_a, \mu_s, g)$ and $T_t(\mu_a, \mu_s, g)$. These approximated R_d and T_t are compared to the measured values. In the case of significant difference, μ_a, μ_s, and g are varied and a next iteration of forward simulation takes place until the difference between measured and simulated R_d and T_t stays in the defined error margin. This process is repeated for all measured wavelengths. A detailed description of the used simulation sequences is described in the work by Friebel et al.[15]

3 Results

Fifty-four fresh tissue samples obtained from five patients during the planned surgery are used for the measurements. As the surgeon has decided based on the local patient anatomy how many and what kind of samples could be extracted, the number of samples differs between the patients and the tissue types. Table 2 shows the number of samples for each tissue type; in average three samples of one tissue type are extracted per patient.

Figure 2 shows the measured reflectance R_d of all six measured tissue types (fat, muscle, parotid gland, nerve, stromal tissue, and tumor). For each tissue type, two measurements are shown. All shown measurements, except for the stromal tissue, share the same setup parameter, in terms of measurement time $t \approx 20$ min, sample size $r \approx 9$ mm, and sample thickness $d = 0.5$ mm. The stromal tissue parameters are $t \approx 35$ min, $r \approx 9$ mm, and $d = 0.16$ mm. The reflectance behavior of each tissue type is consistent, while it differs between the tissue types. The discontinuity at 275 nm results from the change of the light source (deuterium lamp changes to wolfram halogen lamp).

Table 2 The number of extracted tissue samples for each tissue type. On average, three samples per tissue type are extracted from a patient.

	Tissue type					
	Fat	Muscle	Parotid gland	Nerve	Stromal	Tumor
No. of samples	7	7	20	11	3	6

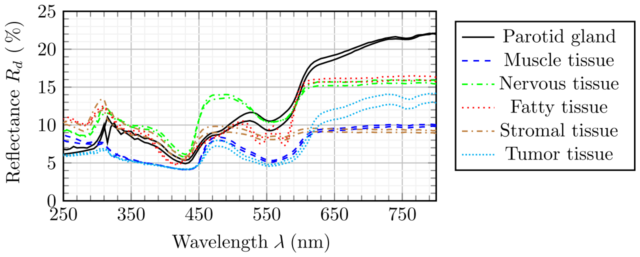

Fig. 2 Plot of two selected examples of the measured reflectance R_d of the six analyzed different tissue types. The light source changes at 275 nm from a deuterium lamp to a wolfram halogen lamp, which produces a small discontinuity at that position in some measurements.

The thickness of the samples spreads between $d = 0.10$ and 0.55 mm, which has a certain effect on the results in terms of quantity. Since d plays a role in the simulation due to the step size of the photons, the simulation results of μ_a and μ_s' spread as well. Figure 3 shows the behavior for measurements of seven different samples of two patients with two different sample thicknesses $d = 0.5$ and 0.1 mm. The curves of the probes with equal d underlie normal variation, while a variation in d results in a clearly visible deviation of the results in the UV range. Human tissue is not translucent for UV radiation, which describes the high μ_a and μ_s' in that range (cf. Figs. 4 and 6). Consequently, the thickness d of the sample has a very strong

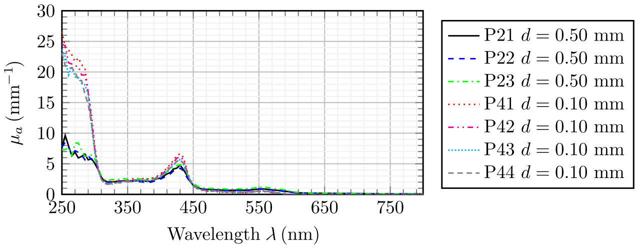

Fig. 3 Plot of the resulting absorption coefficient μ_a of seven different analyzed parotid gland samples of two patients in the measured range of 250 to 800 nm. The sample thickness differs between patients [patient 1 (P21, P22, and P23) $d = 0.50$ mm and patient 2 (P41, P42, P43, and P44) $d = 0.10$ mm], while all other factors (e.g., time point of measurement and sample size $r = 15$ mm) are relatively similar.

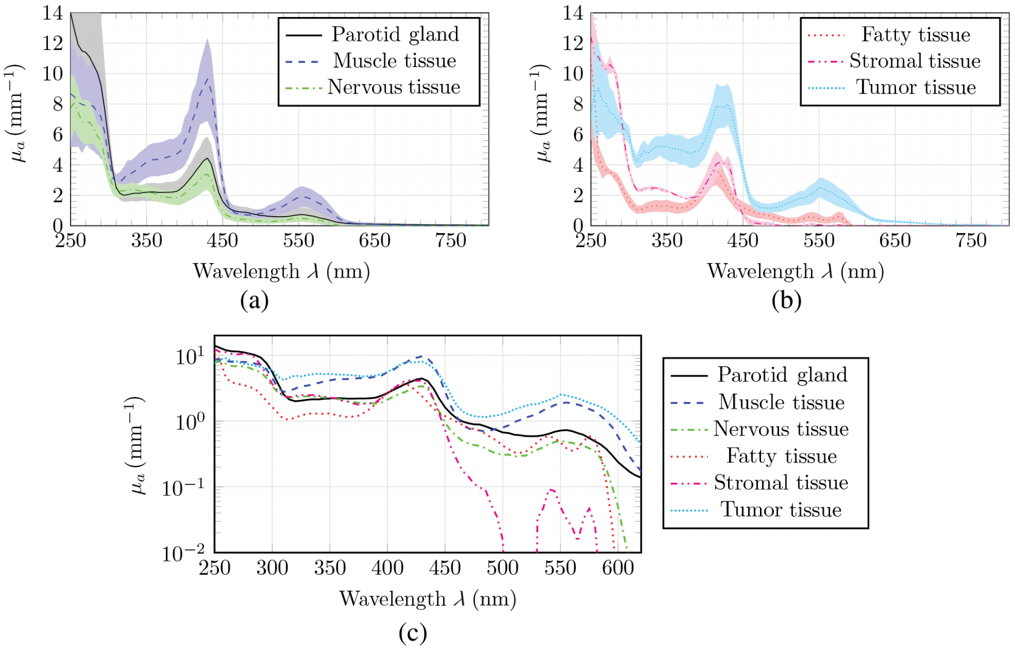

Fig. 4 (a) and (b) Plots of the results of the absorption coefficient μ_a of the six analyzed tissue types in the measured range of 250 to 800 nm. The dark curve shows the average progression of all analyzed probes of each tissue type and the brighter trend characterizes the std of the simulated results. (c) Plot of all results of μ_a in log scale in the range of 250 to 620 nm to better visualize the trends in this visual range.

effect on the measured data in this spectral area. As μ_a is increased for smaller d, the iMCS overestimates the physical effects in the UV range. In the other spectral areas, the deviation is distributed randomly for all different values of d.

Figure 4 shows the average optical absorption coefficient μ_a of parotid gland, muscle tissue, and nervous tissue [in Fig. 4(a)], as well as white adipose tissue, stromal tissue, and tumor [in Fig. 4(b)] in the measured range of 250 to 800 nm. Figure 6 presents the average optical scattering coefficient μ_s' of parotid gland, muscle tissue, and nervous tissue [in Fig. 6(a)], as well as white adipose tissue, stromal tissue, and tumor [in Fig. 6(b)] in the measured range of 250 to 800 nm. The mean relative standard deviations (std) for μ_a and μ_s' over all tissue types are 9.9% (0.099 mm^{-1}) and 8.9% (0.089 mm^{-1}), respectively.

The absorption curves of the samples [cf. Figs. 4(a) and 4(b)] show a characteristic peak between 430 and 440 nm for all tissues indicating characteristic changes in the absorption behavior with the highest average wavelength shift up to $\mu_a = 9.63$ mm^{-1} for muscular tissue. The spread between all samples of muscular tissue is from 65 to 13.59 mm^{-1}. Another unique peak appears at about 555 nm for muscular tissue ($\mu_a = 1.91$ mm^{-1}, spreading from 1.21 to 3.30 mm^{-1}) and tumor tissue ($\mu_a = 2.45$ mm^{-1}, spreading from 1.60 to 3.23 mm^{-1} between all samples). For parotid gland and nervous tissue, this peak is less pronounced with about $\mu_a = 0.73$ mm^{-1} at 555 nm and $\mu_a = 0.50$ mm^{-1} at 550 nm, respectively.

This behavior corresponds to the absorption curve of deoxygenated hemoglobin (Hb) from the literature,[1] which reflects that muscle as well as tumor tissue are strongly supplied with blood, while, e.g., nervous tissue holds less blood. The two peaks at 540 and 575 nm in stromal tissue (0.09 and 0.05 mm^{-1}) as well as in fatty tissue (0.59 and 0.59 mm^{-1}) correspond to oxygenated hemoglobin (HbO_2).[15] Differences in blood supply, oxygen consumption, pH, and temperature of the tissue types could explain this disparity between these two behaviors. Parotid gland, muscle, nerve, and tumor refer to Hb, while stromal and fatty tissue correspond to HbO_2. As described by Boushel et al.,[21] the saturation of O_2 in an organ depends on its current blood flow and work intensity. In addition to the fact that surgery affects the blood supply of the situs in an unforeseen manner, blood flow and oxygen consumption of organs and their enclosing tissues underlay various dynamic regulatory mechanisms.[22] Further, pH and temperature play a substantial role for the HbO_2 and $HbCO_2$ dissociation curves.[23] Thus, one further factor for the missing predominance of HbO_2 in some tissues could be the differences in the pH values. Due to the fact that there are no additional measurements of the mentioned blood parameters of the examined tissues, the exact reason for this finding could not been conclusively clarified.

Starting at about 600 nm, μ_a is decreasing homogeneously in the NIR range, which also corresponds to literature regarding blood analysis.[1] For better visualization of the optical tissue coefficients in the range of 300 to 600 nm, which is the relevant range for intraoperative analysis, Fig. 4(c) shows the curves in logarithmic scale to point out interesting behavior. All coefficients remain approximately constant between 300 and 400 nm. Parotid gland, nerve, and stromal tissue are at about $\mu_a = 2$ mm^{-1}, while muscle and tumor are increased and fat is lower ($\mu_a \approx 0.5$ mm^{-1}). After the described peak at about 430 nm, first stromal tissue decreases rapidly, while fat, stromal, and nervous tissue decrease rapidly at 600 nm.

As the reflectance R_d and transmission T_t measurements of the samples are performed directly after extraction and the amount and type of the extracted tissues differ from patient to patient, each sample is analyzed at different time instants t. Further, some tissue samples have been large enough to be analyzed at several different sample regions. In Fig. 5, six spectra of nervous tissue samples, each measured at three different time instants t, are shown. As is seen, the effect of degeneration has an effect on the optical absorption behavior μ_a; μ_a decreases

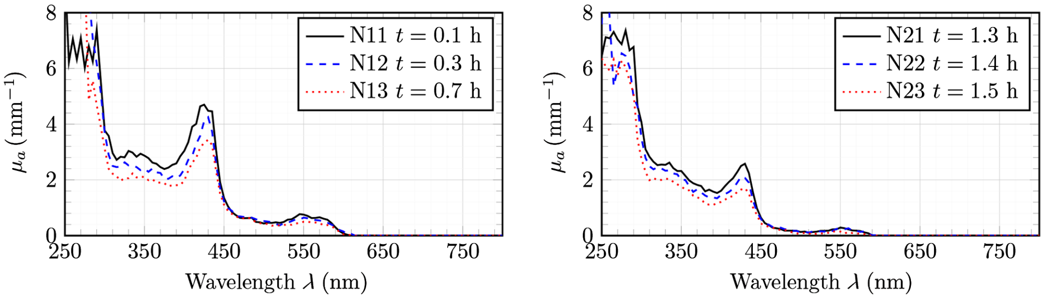

(a)

(b)

Fig. 5 These plots show the resulting absorption coefficient μ_a of two analyzed nervous tissue samples of two patients, each measured at three different time instants t, (a) N11, N12, and N13 of patient 1 and (b) N21, N22, and N23 of patient 2, in the range of 250 to 800 nm. The measurement time t differs between $t = 0.1$ and 1.5 h, while all other factors (e.g., sample thickness $d = 0.362$ mm and size $r = 6.6$ mm) are fixed.

Table 3 The analyzed muscle data with the four muscle data points published in literature.[11] The basic behavior and trend of the measured and literature data are the same but show a constant offset of approximately $+0.03$ for μ_a and -0.2 for μ_s'.

	λ (nm)					
	630	633	635	700	750	800
μ_a, measured (mm^{-1})	0.130	—	0.122	0.022	0.010	0.001
μ_a, Bashkatov et al.[11] (mm^{-1})	—	0.123	—	0.048	0.041	0.028
μ_s', measured (mm^{-1})	1.18	—	1.18	1.02	0.955	0.896
μ_s', Bashkatov et al.[11] (mm^{-1})	—	0.894	—	0.818	0.771	0.704

with increasing degeneration time in the near-UV and visual range (from 300 nm upward). The scattering behavior does not show such effect. This behavior of absorption and scattering corresponds to published mouse data.[6]

For comparison with data from the literature, the absorption spectra of fatty tissue are analyzed. The measured curve for fatty tissue [cf. Fig. 4(b), dotted curve] corresponds well to the published data points in the literature.[11,12,14] Additionally, the average coefficients of muscle [cf. Fig. 4(a), dashed curve] correspond very well to the single sample measurement from Simpson et al.,[13] and the four extracted data points[11] (633, 700, 750, and 800 nm) of μ_a and μ_s' fit to our measured data (see Table 3); however, they show a constant offset caused by the measurement and equipment uncertainties.

The scattering curves of the six analyzed tissue samples [see Figs. 6(a) and 6(b)] show the effective scattering coefficient $\mu_s' = \mu_s(1 - g)$. At 600 nm, μ_s' is in the range between 1.19 mm^{-1} (with std of 0.196 mm^{-1}) for fatty tissue and 2.35 mm^{-1} (with std of 0.392 mm^{-1}) for parotid gland, and it decreases continuously with increasing wavelength. In the NIR range, the curves of muscle, fat, and stromal tissue almost or exactly overlap, while the curves of parotid gland and nerve overlap in the visual range of 490 to 600 nm (green to orange) and start to continuously decrease in that region. Thus, there are not many differences present between the individual soft tissue types in the red and NIR range, which makes it difficult to distinguish between the single tissue types. Only small offsets are visible between some types, while tumor and stromal tissues as well as fatty and muscle tissues or parotid gland and nerve almost overlap.

In the visual and near-UV range, several characteristics are present (cf. Fig. 6). As reported in literature,[24] these characteristics correspond to the behavior of the anisotropy factor g. Stromal and fatty tissues show small double peaks at 550/565 nm with $\mu_s' = 2.25/2.13$ mm^{-1} for stromal tissue and at 540/575 nm with $\mu_s' = 1.51/1.47$ mm^{-1} for fatty tissue. These peaks correspond to μ_s' of HbO$_2$. Tumor and muscle tissues only show a single peak at 550 nm with $\mu_s' = 2.24$ mm^{-1} for tumor and at 555 nm with $\mu_s' = 1.95$ mm^{-1} for muscle, respectively. This single peak corresponds to μ_s' of Hb.

Additionally, all analyzed tissue types hold a distinct peak in the range of 415 nm (fat, $\mu_s' = 3.26$ mm^{-1}) to 430 nm (muscle, $\mu_s' = 6.88$ mm^{-1}, and parotid gland, $\mu_s' = 4.59$ mm^{-1}). Interestingly, tumor tissue shows a double peak at 415/430 nm with $\mu_s' = 5.85/5.82$ mm^{-1}. For stromal tissue, the peak is at 420 nm with $\mu_s' = 4.93$ mm^{-1}, and for nerve, the peak is located at 425 nm with $\mu_s' = 4.97$ mm^{-1}. This different behavior makes this spectral region (visual and near-UV) interesting for intraoperative analysis and distinct tissue differentiation.

The average percentage std over the whole analyzed spectrum for the six tissue ranges from 11.98% (for stromal tissue) and 12.65% (for tumor) to 18.13% (for fat) and 21.89% (for muscle). Parotid gland and nerve hold a std of 17.76% and 17.61%, respectively. The highest deviation occurs in the near-UV range (between 250 and 295 nm) for all six analyzed tissue types. The smallest deviation is always achieved in the visual spectrum (up to 780 nm).

4 Discussion and Conclusion

In this study, a high precision integrating sphere setup for measuring R_d and T_t in combination with a high resolving iMCS is used to determine the intrinsic optical parameters μ_a and μ_s' of human soft tissue (fat, muscle, parotid gland, nerve, stromal tissue, and tumor tissue) in the wavelength range of 250 to 800 nm. This is in contrast to most of the results on tissue behavior presented in the literature, which mostly concern the IR range. As the visual range is of high interest to the surgeon for carrying out daily diagnostic and therapeutic interventions with or without microscopic and endoscopic support, this is the spectral range of interest in this study.

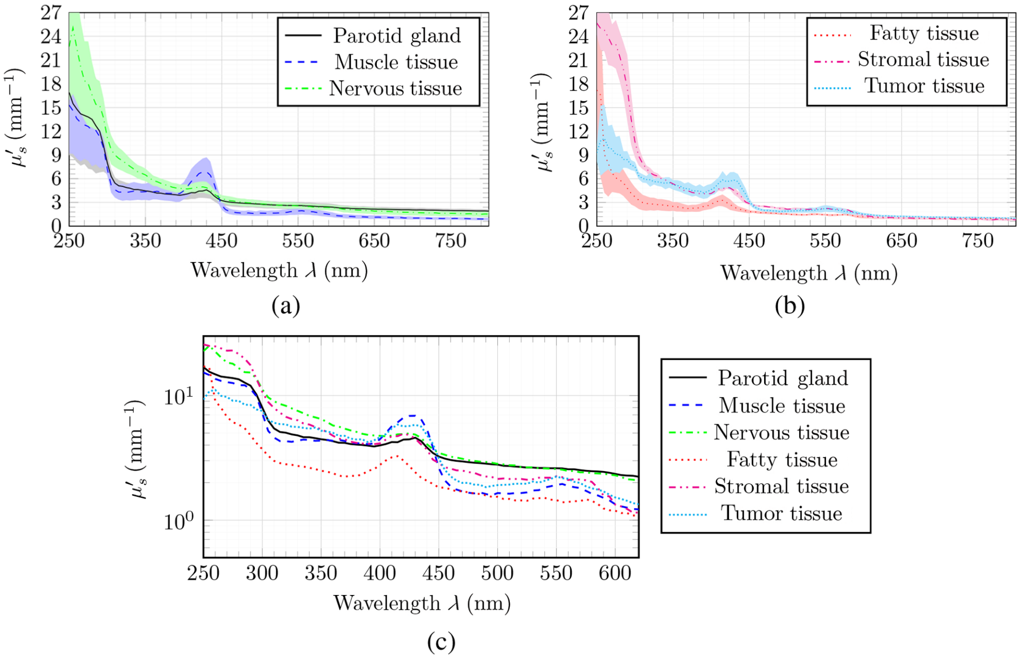

(a) (b)

(c)

Fig. 6 (a) and (b) Plots of the results of the scattering coefficient μ_s' of the six analyzed tissue types in the measured range of 250 to 800 nm. The dark curve shows the average progression of all analyzed probes of each tissue type and the brighter trend characterizes the spread of the simulated results. (c) Plot of all results of μ_s' in log scale in the range of 250 to 620 nm to better understand the trends in this visual range.

Although the first published results on fat, blood, and skin have already been shown, there is still insufficient data for the tissue types that are important to clinicians and surgeons, such as nerve and gland tissues and in particular different types of tumors and chronic inflammation. This study reduces this gap significantly. However, this study has some limitations: no real *in-vivo* measurements were possible due to the measurement setup, which is a limitation for further intraoperative analyses. In addition, it was not possible to extract every tissue type from all patients. As a result, stromal and tumor tissues are each only analyzed from a single patient. Consequently, only one tumor type is examined in this study. The tumor sample is from a cystadenolymphoma. It is supposed that different tumor types show variance in μ_a and μ_s', because they consist of different cell types. This means that the results of parotid tumor tissue acquired in this study only can be a representative for cystadenolymphoma.

All tissue types show characteristic peaks for μ_a and μ_s' corresponding to the behavior of hemoglobin. These peaks vary in intensity depending on the type of tissue. For tissue with high blood flow (e.g., muscle and tumor), more pronounced peaks could be observed than for tissue with low blood flow (e.g., nerve). As it was not possible to control blood parameter as the actual blood flow, oxygen consumption, and pH of the specimen during surgery, while extracting the samples, the corresponding oxygenation status could not be determined. Therefore, this study cannot conclusively clarify why some tissue types hold the single peak of deoxygenated Hb in the absorption spectrum and other tissue types hold the double peak of oxygenated Hb.

Since no *in-vivo* measurements are possible due to the measurement setup, but the *in-vivo* tissue properties are of clinical interest, the samples are prepared and measured immediately after collection. In addition, it is shown that degeneration of the tissue causes the absorption coefficient μ_a to drop. Thus, the principle *in-vivo* tissue properties can be deduced from the presented results, as the measurements are carried out next to the surgery site with minimal time delay.[6]

We have shown that fundamental variances exist for the investigated tissue types in the visual range. Especially from 300 to 600 nm, large differences in the specific tissue behavior (i.e., the measured reflectance values R_d as well as the determined optical parameters μ_a and μ_s') can be detected.

These differences in the optical parameters substantiate the validity to detect and identify, automatically or semiautomatically, tissue types for active treatment decisions during image-guided surgery.[2,25,26] Intraoperative tissue properties can be analyzed using multispectral imaging to point out tissue differences in the visualization process using the knowledge acquired in this study. By contrast, it seems possible to use the results presented here to learn a classifier that makes tissue types more distinguishable intraoperatively.

Disclosures

No conflicts of interest, financial or otherwise, are declared by the authors.

Acknowledgments

This work was supported by the VW Foundation (Grant No. 93927) as well as the Federal Ministry of Education and Research (BMBF, Grant No. 16SV8061) and was presented at the SPIE/OSA European Conference of Biomedical Optics (ECBO) 2019 in Munich, Germany. The authors wish to thank the Center of Experimental and Applied Cutaneous Physiology, Charité–Universitätsmedizin, Campus Mitte, Berlin, Germany, as well as Professor Dr. Meinke for providing the spectrometer and having such fruitful discussions.

References

1. S. L. Jacques, "Optical properties of biological tissues: a review," *Phys. Med. Biol.* **58**(11), R37–R61 (2013).
2. E. L. Wisotzky et al., "Intraoperative hyperspectral determination of human tissue properties," *J. Biomed. Opt.* **23**(9), 091409 (2018).
3. E. L. Wisotzky et al., "Validation of two techniques for intraoperative hyperspectral human tissue determination," *Proc. SPIE* **10951**, 109511Z (2019).
4. J. E. East et al., "Advanced endoscopic imaging: European Society of Gastrointestinal Endoscopy (ESGE) technology review," *Endoscopy* **48**(11), 1029–1045 (2016).
5. W.-F. Cheong, S. A. Prahl, and A. J. Welch, "A review of the optical properties of biological tissues," *IEEE J. Quantum Electron.* **26**(12), 2166–2185 (1990).
6. E. Salomatina and A. Yaroslavsky, "Evaluation of the in vivo and ex vivo optical properties in a mouse ear model," *Phys. Med. Biol.* **53**(11), 2797–2807 (2008).
7. B. M. Tissue, Ultraviolet and visible absorption spectroscopy in *Characterization of Materials*, 1st ed., Vol. 2, pp. 688–698, Virginia Polytechnic Institute and State University, Blacksburg, Virginia (2002).
8. M. C. Meinke et al., "Optical properties of platelets and blood plasma and their influence on the optical behavior of whole blood in the visible to near infrared wavelength range," *J. Biomed. Opt.* **12**(1), 014024 (2007).
9. S. L. Jacques and B. W. Pogue, "Tutorial on diffuse light transport," *J. Biomed. Opt.* **13**(4), 041302 (2008).
10. B. J. Tromberg et al., "Non-invasive measurements of breast tissue optical properties using frequency-domain photon migration," *Phil. Trans. R. Soc. Lond. B* **352**, 661–668 (1997).
11. A. N. Bashkatov, E. A. Genina, and V. V. Tuchin, "Optical properties of skin, subcutaneous, and muscle tissues: a review," *J. Innovative Opt. Health Sci.* **4**(1), 9–38 (2011).
12. G. Alexandrakis, F. R. Rannou, and A. F. Chatziioannou, "Tomographic bioluminescence imaging by use of a combined optical-PET (OPET) system: a computer simulation feasibility study," *Phys. Med. Biol.* **50**(17), 4225–4241 (2005).
13. C. R. Simpson et al., "Near-infrared optical properties of *ex vivo* human skin and subcutaneous tissues measured using the Monte Carlo inversion technique," *Phys. Med. Biol.* **43**(9), 2465–2478 (1998).
14. E. V. Salomatina et al., "Optical properties of normal and cancerous human skin in the visible and near-infrared spectral range," *J. Biomed. Opt.* **11**(6), 064026 (2006).
15. M. Friebel et al., "Determination of optical properties of human blood in the spectral range 250 to 1100 nm using Monte Carlo simulations with hematocrit-dependent effective scattering phase functions," *J. Biomed. Opt.* **11**(3), 034021 (2006).
16. A. Roggan et al., "Optical properties of circulating human blood in the wavelength range 400–2500 nm," *J. Biomed. Opt.* **4**(1), 36–47 (1999).
17. A. N. Yaroslavsky et al., "Optical properties of blood in the near-infrared spectral range," *Proc. SPIE* **2678**, 314–324 (1996).
18. J. W. Eveson et al., *Tumours of the Salivary Glands: Introduction*, Vol. 9, Chapter 5, pp. 212–215, IARC Press, Lyon, France (2005).
19. A. Roggan, "Measurements of optical tissue properties using integrating sphere technique," *Proc. SPIE* **10311**, 103110A (1993).
20. W. H. Press et al., *Numerical Recipes in Pascal: The Art of Scientific Computing*, Vol. 1, Cambridge University Press, Cambridge (1989).
21. R. Boushel et al., "Monitoring tissue oxygen availability with near infrared spectroscopy (NIRS) in health and disease," *Scand. J. Med. Sci. Sports* **11**(4), 213–222 (2001).
22. D. L. Boveris and A. Boveris, "Oxygen delivery to the tissues and mitochondrial respiration," *Front. Biosci.* **12**(3), 1014–1023 (2007).
23. R. K. Dash and J. B. Bassingthwaighte, "Blood HbO_2 and $HbCO_2$ dissociation curves at varied O_2, CO_2, pH, 2, 3-DPG and temperature levels," *Ann. Biomed. Eng.* **32**, 1676–1693 (2004).
24. M. Friebel et al., "Influence of oxygen saturation on the optical scattering properties of human red blood cells in the spectral range 250 to 2000 nm," *J. Biomed. Opt.* **14**(3), 034001 (2009).
25. E. Wisotzky et al., "A hyperspectral method to analyze optical tissue characteristics *in vivo*," *Int. J. Comput. Assisted Radiol. Surg.* **13**, S46–S47 (2018).
26. J.-C. Rosenthal et al., "Interactive and multimodal-based augmented reality for remote assistance using a digital surgical microscope," in *IEEE VR Workshop Appl. VR Enhanced Healthcare*, Vol. 26, pp. 1–9 (2019).

Eric L. Wisotzky received his BSc and MSc degrees from Heidelberg University, Germany, in 2012 and 2014, respectively. After a research visit at Sydney Medical School, Sydney University, he is currently working toward his doctoral degree at Humboldt University of Berlin and Fraunhofer Heinrich-Hertz-Institute. Together with the Department of Otolaryngology of Charité–Universitätsmedizin Berlin, he is working on new image-guided surgery techniques. His research interests span from imaging physics to image processing and modeling in medicine. He is a member of SPIE.

Peter Eisert is a professor of visual computing at Humboldt University Berlin and the head of the Vision and Imaging Technologies Department, Fraunhofer HHI, Germany. He received his Dr.-Ing. degree from the University Erlangen in 2000 and worked as a postdoctoral fellow at Stanford University. He is coordinating and initiating numerous research projects on image/video analysis and synthesis, face processing, computer vision, and graphics in multimedia, security, and medical applications. He has published more than 150 conference and journal papers and is a associate editor of *Journal on Image and Video Processing* and *Journal of Visual Communication and Image Representation*.

Biographies of the other authors are not available.